A&A 435, 563–574 (2005)
DOI: 10.1051/0004-6361:20042235

Astronomy & Astrophysics

The mid-IR spatially resolved environment of OH 26.5+0.6 at maximum luminosity⋆

O. Chesneau[1], T. Verhoelst[2], B. Lopez[3], L. B. F. M. Waters[2,4], Ch. Leinert[1], W. Jaffe[5], R. Köhler[1], A. de Koter[4], and C. Dijkstra[4]

[1] Max-Planck-Institut für Astronomie, Königstuhl 17, 69117 Heidelberg, Germany
e-mail: chesneau@mpia-hd.mpg.de
[2] Insituut voor Sterrenkunde, KU Leuven, Celestijnenlaan 200B, 3001 Leuven, Belgium
[3] Observatoire de la Côte d'Azur-CNRS-UMR 6203, Boulevard de l'Observatoire, BP 4229, 06304 Nice Cedex 4, France
[4] Astronomical Institute "Anton Pannekoek", University of Amsterdam, Kruislaan 403, 1098 SJ Amsterdam, The Netherlands
[5] Sterrewacht Leiden, Niels-Bohr-Weg 2, 2300 RA Leiden, The Netherlands

Received 22 October 2004 / Accepted 12 January 2005

Abstract. We present observations of the famous OH/IR star OH 26.5+0.6 obtained using the Mid-Infrared Interferometric Instrument MIDI at the European Southern Observatory (ESO) Very Large Telescope Interferometer VLTI. Emission of the dusty envelope, spectrally dispersed at a resolution of 30 from 8 μm to 13.5 μm, appears resolved by a single dish UT telescope. In particular the angular diameter increases strongly within the silicate absorption band. Moreover an acquisition image taken at 8.7 μm exhibits, after deconvolution, a strong asymmetry. The axis ratio is 0.75 ± 0.07 with the *FWHM* of the major and minor axis which are 286 mas and 214 mas respectively. The measured PA angle, 95° ± 6°, is reminiscent of the asymmetry in the OH maser emission detected at 1612 MHz. In interferometric mode the UT1−UT3 102 m baseline was employed to detect the presence of the star. No fringes were found with a detection threshold estimated to be about 1% of the total flux of the source, i.e. 5−8 Jy. These observations were carried out during the maximum luminosity phase of the star, when the dust shell is more diluted and therefore the chance to detect the central source maximized. We modeled the dusty environment based on the work of Justtanont et al. (1996). In particular, the failure to detect fringes provides strong constraints on the opacities in the inner regions of the dust shell or in the close vicinity of the star.

Key words. radiative transfer – techniques: interferometric – stars: AGB and post-AGB – stars: circumstellar matter – stars: individual: OH 26.5+0.6

1. Introduction

The short transition phase between the end of the Asymptotic Giant Branch (AGB) phase and the formation of a White Dwarf (WD) surrounded by a Planetary Nebula (PN) is still poorly understood. The drastic changes observed in the circumstellar environment of AGB and post-AGB stars are particularly puzzling. During the late AGB or early post-AGB evolutionary stages, the geometry of the circumstellar material of the vast majority of stars changes from more or less spherical to axially symmetric, as shown by the large number of axisymmetric proto-PNe (e.g. Sahai 2000). As a result, most PNe exhibit axisymmetric structures, ranging from elliptical to bipolar, often with an equatorial waist and (sometimes multiple) jets (Corradi & Schwarz 1995). It is thought that the pure hydrodynamical collimation provided by dense equatorial disks or tori (Icke et al. 1989) and/or magneto-hydrodynamical collimation (Chevalier & Luo 1994) can explain the development of the extreme bipolar geometries observed. Whether these equatorial structures can arise in a single star scenario is still strongly debated (Bujarrabal et al. 2000).

In recent years the advent of infrared spectroscopy has improved our understanding of the AGB and post-AGB evolutionary phase. The IRAS and the ISO infrared telescopes have detected large amounts of dust grains around these stars. The majority of observed circumstellar environments show either an oxygen-rich chemistry or a carbon-rich one. AGB/post-AGB stars dominated by O-rich dust chemistry are those where the third dredge-up never raised the C/O ratio above 1. During the AGB phase, mass loss drives the evolution of the star. In particular, mass loss increases dramatically (by a factor 10 at least) towards the tip of the AGB in what is called a superwind (Iben & Renzini 1983), which ejects most of the remaining envelope of the star. Some O-rich AGB stars exhibit OH maser emission and are called OH/IR stars (Wilson & Barrett 1972). Their mass-loss rates are so high that the dust shell completely obscures the central star, and the object is observable only at infrared wavelengths and through molecular line emission at

⋆ Based on observations made with the Very Large Telescope Interferometer at Paranal Observatory.

radio wavelengths. The nature and geometry of the superwind still has to be settled. The geometry of the maser emission is usually well constrained due to the combination of spatial resolution provided by interferometric techniques and large extension of the maser (usually a few arcsec). Observations of the youngest (i.e. more optically obscured) pre-planetary nebulae (PPN), where the superwind has just ceased, suggest that asymmetries are already present. An extensive discussion of the appearance of bipolar outflows in OH/IR stars can be found in Zijlstra et al. (2001).

OH 26.5+0.6 (RAFGL 2205, IRAS 18348-0526) is an extreme OH/IR star showing large dust column density, hence a very high dust mass loss rate. It is one of the brightest OH maser emitters (Baud 1981; te Lintel Hekkert et al. 1989; Bowers & Johnston 1990) with a wind terminal velocity of 15 $\mathrm{km\,s^{-1}}$. Bowers & Johnston (1990) mapped the OH maser around the star and found a shell radius of about 2−3 arcsec. OH 26.5+0.6 exhibits a low CO $J = 1-0$ and $J = 2-1$ emission (Heske et al. 1990), while at 10 μm, the silicate absorption indicates large dust column density so a very high dust mass loss rate. The 10 μm complex is dominated by amorphous silicate absorption, which has been studied by numerous authors. The ISO spectrum of OH 26.5+0.6 was discussed by Sylvester et al. (1999) while Molster et al. (2002) studied the signature of the crystalline silicates in particular.

Justtanont et al. (1994, 1996, hereafter JU96) suggested that this star has recently undergone the superwind phase and shows evidence of two mass-loss regimes: a superwind phase in which the mass-loss rate is 10^{-4} $M_{\odot}$/yr, which started recently ($t < 150$ yr), and an earlier AGB phase with a mass-loss rate of about 10^{-6} $M_{\odot}$/yr. The integrated mass lost during the superwind phase has been estimated to be 0.1 $M_{\odot}$.

Fong et al. (2002) reported millimetric CO observations which did not show any significant deviation from spherical symmetry for the envelope of OH 26.5+0.6. Nevertheless, it must be pointed out that the source is mainly unresolved at this wavelength. In contrast, it is one of the brightest and most asymmetric OH maser sources known among AGB stars with a preferential axis of symmetry oriented approximately east-west (Baud 1981; Bowers & Johnston 1990).

The duration of the superwind phase depends on the mass that the star has to lose before the envelope is small enough to sustain the mechanism of stellar (photospheric) pulsations. For a star like OH 26.5+0.6, JU96 state that the superwind *began very recently i.e. less than 150 yr ago*. Radio emission in molecular lines is expected to change less rapidly than infrared emission at the advent of the superwind phase. It is therefore of particular interest to study the mid-IR spatial geometry of OH/IR stars, in order to determine the onset of asymmetries in the environment of evolved stars.

Unfortunately, the dusty environment of OH/IR stars is difficult to resolve by single dish telescopes in the IR. Even more complicating is the time variability of those OH/IR envelopes that modulate their size and luminosity. OH 26.5+0.6 is a long period pulsating star, whose period has been refined recently by Suh & Kim (2002) to $P = 1559 \pm 7$ days. The published data on the IR spatial extent of OH 26.5+0.6 have to be systematically placed in their temporal context owing to the large variations of the IR flux from this star throughout its pulsation cycle. Infrared speckle interferometry was performed by Fix & Cobb (1988) close to the maximum. They provide an angular diameter for the circumstellar dust shell at 9.7 μm (within the strong silicate absorption) at maximum of $0.5'' \pm 0.02''$, while outside this feature (at 8 μm) the shell remained unresolved by their experiment (at most $0.2''$). They also resolved the environment using the broad N band filter near phase 0.6 with a detected *FWHM* of about $0.3''$ (Cobb & Fix 1987). Some asymmetries have been reported by Mariotti et al. (1982), Dyck et al. (1984), Cobb & Fix (1987), Fix & Cobb (1988) and Starck et al. (1994). However, reported asymmetries are within the estimated error bars of the measurements and altogether the results are somewhat inconclusive and sometimes contradictory.

The Mid-Infrared Interferometric Instrument MIDI attached to the Very Large Telescope Interferometer (VLTI) is able to provide spatial resolution in the mid-infrared, ranging from the one provided by single-dish 8 m telescope (about 300 mas) to the one provided by interferometric technique (about 5−10 mas). MIDI can also disperse the light with a spectral resolution of 30 through the entire N band, which makes it a unique instrument particularly adapted to the study of dusty environments. We used the 102 m baseline between the telescopes Antu (UT1) and Melipal (UT3) to observe OH 26.5+0.6 for the first time.

In Sect. 2 we describe the observations and the data reduction procedures in three parts: (i) single dish acquisition images (Sect. 2.1); (ii) spatial and spectral information on the spectra (Sect. 2.2); and (iii) the interferometric signal (Sect. 2.3). In Sect. 3 we model the observations using a spherically symmetric dust model. Finally, in Sect. 4 we discuss the results of our model fitting.

2. Observations and data reduction

OH 26.5+0.6 was observed with MIDI (Leinert et al. 2003a,b), the mid-infrared recombiner of the VLTI. The VLTI/MIDI interferometer operates as a classical Michelson stellar interferometer to combine the mid-IR light (N band, 7.5−14 μm) from two VLT Unit Telescopes (UTs). The observations presented here were conducted on the night of 14 of June 2003, during which the UT1 and the UT3 telescopes were used, separated by 102 m with the baseline oriented 40° (East of North).

The observing sequence, described extensively in Przygodda et al. (2003), is summarized hereafter. The images were recorded using the MIDI star acquisition modes called Default_Chop and Acquisition_chop with the 8.7 μm filter. The Acquisition_Chop mode is the first template used after the pointing to test if the target is within the MIDI Field Of View (FOV) (diameter of about $3''$) and to perform a fine pointing. The chopping mode ($f = 2$ Hz, angle −90 degree) is used to visualize the star, which is not perfectly centered in the first image and then centered in a second step. The number of frames recorded per image is usually about 2000 and the exposure time is by default 4 ms, in order to avoid background saturation. If the result of the template is not satisfactory, the procedure is started over. It must be pointed out that no nodding sequences are performed for technical reasons and the

sky is removed by chopping alone. For some stars for which the coordinates are not well-defined, it might be difficult to get the star directly in the MIDI FOV on the first try, which was the case for OH 26.5+0.6. Therefore, a particular acquisition mode is used instead. In this mode, images are recorded only for visualization, and the pointing is done by "hand" between or sometimes during exposures. In this mode, the number of frames is larger, 15 000 frames in our case. The cycle rate is close to 10 ms, so we recorded 15 000 frames in about 2.5 min. We stress that MIDI is not intended as an imager instrument but as a long-baseline interferometer. Therefore the majority of the targets are totally unresolved by a single 8 m telescope, providing a wealth of instrumental Point Spread Function (PSF) images. The PSF files were recorded with the normal Acquisition_Chop automatic mode and contain 2000 frames (20 s).

In the following section we present the deconvolution treatment applied to the acquisition images.

2.1. Images

Data used to obtain a deconvolved image of OH 26.5+0.6 are summarized in Table 1. The observations were recorded during the acquisition process and the source location within the field of view can be different for each file. The PSFs are generally well-centered except for PSF#1. STAR#1 was very far from the FOV center, and the quality of the deconvolution using this observation is very low but note that the results are consistent with the other measurements.

Numerous observations of two PSFs (HD 168454 and HD 177716) were performed before and after the star acquisition. HD 168454 is a bright K3IIIa star exhibiting an IRAS 12 μm flux of 62 Jy (the IRAS flux of OH 26.5+0.6 is 360 Jy). HD 177716 is a K1IIIb that was observed by IRAS with a flux of 26.9 Jy. There is a Cohen template available from the ISO primary calibration database[1] (Cohen et al. 1999). The visual seeing during the HD 168454 exposures was ∼0.″4; during the OH 26.5+0.6 exposures it was ∼0.″5, and during the HD 177716 around 0.″6. The airmass of the three targets ranges between 1 to 1.16. The pixel size on the sky is 98 mas, a scale factor defined from the MIDI observations of close visual binaries.

The deconvolution was performed using the Lucy-Richardson algorithm (1974) embedded in the IDL astrolib package developed by NASA. Choosing the right iteration number for the Lucy-Richardson algorithm is always a difficult task. Our goal is clearly not to perform the "best" deconvolution possible but to increase the spatial resolution of the image that is well resolved by the UTs. The number of iterations used was between 40 and 60. The levels where the different deconvolved images begin to disagree are between 0.3% and 1% of the maximum flux of the image, depending on the quality of measurement. The level of the differences between PSF#1 and PSF#6 is about 0.3%. The level of the differences between the PSFs of HD 168454 and those from HD 177716 can reach 2% for an individual deconvolution but is usually 1%. PSF#7 and PSF#8 are quite different, with a level of residuals reaching 1.5%.

[1] http://www.iso.vilspa.esa.es/users/expl_lib/ISO/wwwcal/

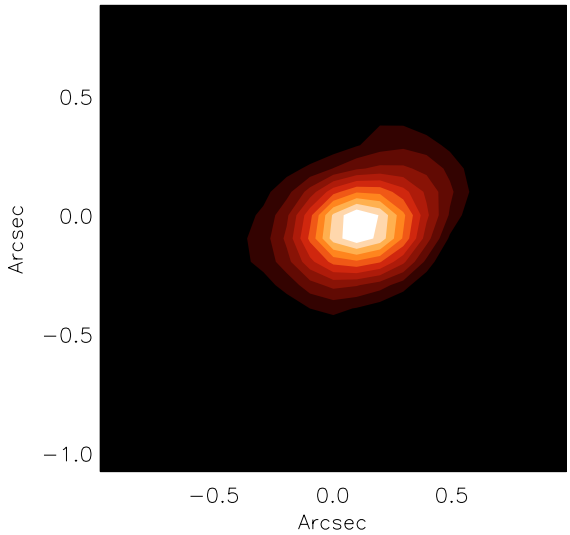

Fig. 1. Contours of the mean of STAR#3 and STAR#4 deconvolved images. The contour levels are linearly spaced for the double square root of the image $I^{1/4}$. The last contour is equivalent to 25% of the maximum of $I^{1/4}$, i.e. 0.4% of the maximum of I. The three last contours are the most susceptible to reconstruction artifacts. The North is up and the east to the left.

Table 1. Journal of observations: acquisition images.

Star	Name	Time	Frames	t_{exp}
HD 168454	PSF#1	06:02:09	2000	20 s
HD 168454	PSF#2	06:03:49	2000	20 s
HD 168454	PSF#3	06:07:34	2000	20 s
HD 168454	PSF#4	06:08:39	2000	20 s
HD 168454	PSF#5	06:14:40	2000	20 s
HD 168454	PSF#6	06:15:50	2000	20 s
OH 26.5+0.6	STAR#1	06:56:24	10 000	100 s
OH 26.5+0.6	STAR#2	07:00:02	5000	50 s
OH 26.5+0.6	STAR#3	07:03:46	15 000	150 s
OH 26.5+0.6	STAR#4	07:07:30	15 000	150 s
HD 177716	PSF#7	08:03:11	2000	20 s
HD 177716	PSF#8	08:04:23	2000	20 s

Statistical properties of the PSFs were carefully inspected and a sub-set of good ones (5 over 8) have been selected for deconvolution. Each data set was deconvolved using the good PSFs, and we examined the statistics of their geometrical characteristics. A mean deconvolved image was created using the mean image of STAR#3 and STAR#4, which were located at the same place in the detector. This reconstructed image is shown in Fig. 1 to illustrate the quality of the reduction process. The position of the target for the two other files was different and we did not attempt any shift-and-add procedure to create a single mean image, since the useful information is extracted from the properties individual images. We performed a 2D Gaussian fit for each mean deconvolved image which provides the image position, extension and the angle of the long

Table 2. Image size statistics.

Name	*FWHM X* (mas)	rms (mas)	*FWHM Y* (mas)	rms (mas)
PSF#4	148	24	148	24
PSF#6	150	28	142	20
PSF#8	160	26	166	22
STAR#1	214	8	286	18
STAR#2	210	2	292	14
STAR#3	218	4	296	16
STAR#4	212	2	268	12

Table 3. Deconvolved image parameters.

Parameter	Mean	rms
Mean radius	240 mas	±14
Mean *X* axis	214 mas	±4
Mean *Y* axis	286 mas	±6
Mean ratio	0.75	±0.07
Mean PA angle	95°	±6°

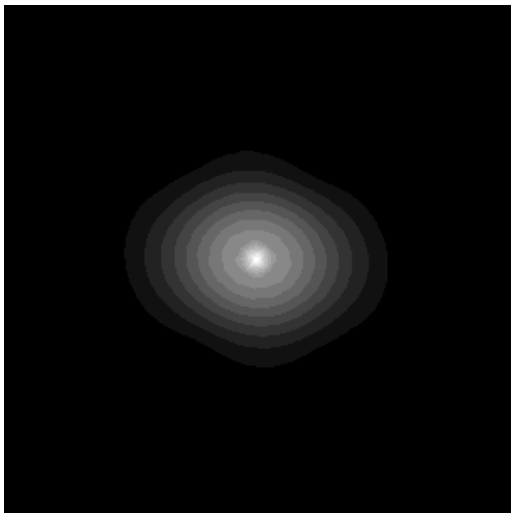

Fig. 2. Contours of the reconstructed *L* image from the speckle observations at the ESO 3.6 m telescope on La Silla (courtesy of Starck et al.). The contour levels are linearly spaced for the square root of the image $I^{1/2}$.

axis on the detector frame. Table 2 presents the statistics of this 2D Gaussian procedure and Table 3 presents the mean parameters of the deconvolved images.

We are confident that the star is indeed resolved at 8.7 μm, as is definitely settled by looking at the *FWHM* of the spectra (Sect. 2.2). However, it is necessary to carefully check whether the asymmetry of the image is real or not. The image asymmetry is so obvious that we can be certain of its detection but the PA angle is almost coincident with the chopping direction. Several checks were performed to ensure this detection:

1. As a comparison, the ratio between *Y* and *X* extension for the PSFs is 0.997 ± 0.05. Moreover the angle of the 2D Gaussian used for the fit fluctuates randomly and there is no indication in the PSF files that the chopping had any influence on the PSF's shape, i.e. that the chopping flagging was uncertain during the exposures.
2. The star is very bright and we tested the deconvolution process in some carefully chosen individual frames (4 ms exposure) taken in the middle of the chopping cycle. The asymmetry is already detectable with SNR larger than 5 in the best quality frames.
3. We have checked in the literature whether such asymmetry could have been detected in NIR by speckle interferometry in the past. Some asymmetries were indeed reported by Mariotti et al. (1982), Cobb & Fix (1987) and Fix & Cobb (1988) in *L*, *M* and *N* bands. However the detected axis ratios are not convincing, usually within the estimated error bars of the measurement and not free of any bias as pointed out by Fix & Cobb (1988). Other speckle measurements in the *L* and *M* bands are reported by Starck et al. (1994) based on observations carried out with the 3.6 m telescope of ESO/La Silla at pulsation phase 0.22 (JD = 2 448 429), i.e. close to maximum luminosity. A strong asymmetry is detected in the *L* band with a N-S/E-W ratio on the order of 0.82 ± 0.03 after removing the unresolved object (Starck, private communication). This measurement was performed with more than 5 orientations on the sky to prevent direction-dependent bias. Agreement between their reconstructed *L* band image and our 8.7 μm image is convincing as shown in Fig. 2.
4. Surprisingly, the asymmetry reported in this paper is also correlated with the strong one reported at 1612 MHz by Bowers & Johnston (1990) on a much larger scale (a few arcsecs). Even more interesting, they reported a rotation of OH 26.5+0.6's shell at low velocity (2−3 km s^{-1}) for which the projected axis is oriented in the north-south direction. This axis is aligned with the minor axis of the *L* and 8.7 μm images, and the consequences of such a correlation will be discussed more extensively in Sect. 4.

Based on the above considerations, we are convinced that the measured flattening is real. The data are not affected by any bias influencing the shape of the resulting images, and this asymmetry was also seen in other independent data sets.

2.2. Spectrum

The photometry extracted from UT1 and UT3 is intended to calibrate the recorded fringes. Two photometric files are recorded for each target. In the first file, only one shutter is opened (corresponding to UT1) and the flux is then split by the MIDI beam splitter and falls onto two different regions of the detector. The same procedure is then applied with UT3. The data used to get photometrically calibrated spectra and fringes of OH 26.5+0.6 is listed in Table 4.

An independent calibration is performed for the individual spectra from each part of the detector and for each telescope. The first step is to read in the photometric data sets, average the frames on the target and the frames on the sky, and subtract the average sky frame from the average target frame. The position

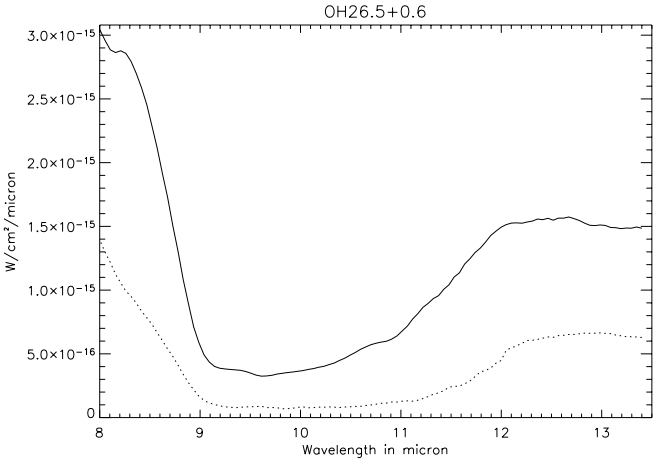

Fig. 3. Calibrated spectrum from MIDI (solid line) corresponding to the mean flux from UT1 and UT3. The flux is almost 300% higher than the flux observed by ISO, shown with a dotted line. The ISO data were recorded during a minimum of the lightcurve.

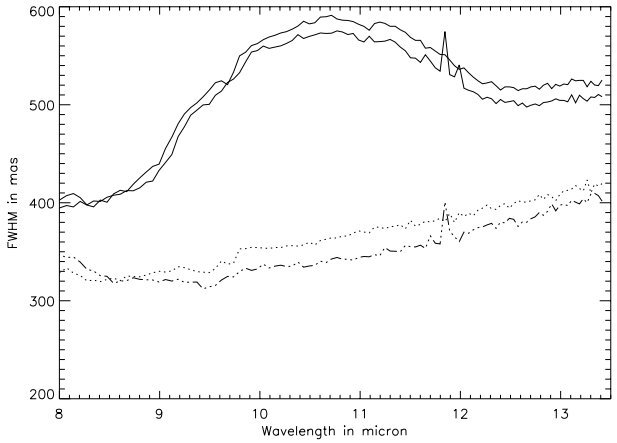

Fig. 4. *FWHM* of the star spectrum from UT1 (solid lines) throughout the wavelength range compared to *FWHM* of the calibrator spectrum of HD 168454 (dotted lines). There are two lines per target because the MIDI beam splitter is inserted and the light falls onto two different regions of the detector.

Table 4. Journal of observations: fringes (Frg) and photometric files (Phot).

Star	Telescope	Time	Frames	File
HD 168454	UT1	06:40:47	3000	Phot
HD 168454	UT3	06:43:12	3000	Phot
OH 26.5+0.6	UT1/UT3	07:13:36	12 000	Frg
OH 26.5+0.6	UT1/UT3	07:20:09	9000	Frg
OH 26.5+0.6	UT1/UT3	07:23:46	9000	Frg
OH 26.5+0.6	UT1	07:27:51	3000	Phot
OH 26.5+0.6	UT3	07:29:51	3000	Phot
HD 177716	UT1	08:18:44	3000	Phot
HD 177716	UT3	08:20:48	3000	Phot

of the spectrum is then measured column-wise by searching for peaks that are sufficiently high above the background fluctuations. The result is the position and width of the spectrum as a function of wavelength.

We use HD 177716 as absolute flux calibrator (Cohen et al. 1999), taking into account differences in air mass between calibrator and OH 26.5. Then, the calibrated spectra are combined in order to provide a high SNR spectrum. The shape of spectra from the same telescope agree within 1−2%; but the spectra from two different telescopes can vary by about 5%, which is due to different optical paths that are intrinsically different during the early use of the MIDI instrument with the VLTI (poor pupil transfer). This defines the limit of relative error in the shape of the spectrum (pixel to pixel and in terms of slope) which was below 5%. This limit was also checked by extracting the spectra of several spectrophotometric calibrators observed by MIDI in several observing runs. The temporal flux variations are the dominant source of error for the absolute flux calibration, and variations of 5−20% or even more are routinely observed in the *N* band. During the night of the OH 26.5+0.6 observations, the photometric errors were limited to 8%.

We studied the spatial extension of the spectra in the direction of the slit in order to check if the shell of OH 26.5+0.6 is spatially resolved at all wavelengths. A 1D Gaussian fit was performed for each column of each spectrum from the target and the calibrators. The PA angle of the slit at 72° is close to the PA angle of the major axis detected in the deconvolved image at 95°. In Fig. 4 we see that OH 26.5+0.6 is well-resolved by the 8m telescope. Moreover the star is much larger in the silicate band. No image sharpening was applied as this result was directly extracted from the mean MIDI spectra.

In order to constrain the true size of the object in the slit direction, we performed a deconvolution on each of the 4 available spectra, two for each telescope. A 1D deconvolution using the Lucy-Richardson algorithm was performed column by column using a normalized column from the calibrators as PSF. The same number of iterations is applied for all the wavelengths. There are systematic differences between the shapes provided by UT1 and UT3 which can be attributed to differences in the optical quality of different light paths.

2.3. Fringes

Fringes were sought by repeatedly scanning a large range of optical path difference between the two telescopes, using a small instrumental delay line (see Leinert et al. 2004, for a description of the observing sequence). The usual data reduction process is the following: a mask is created with the average position and width of the spectra recorded in the photometric files for UT1 and UT3. This mask is used to extract the object data from the fringe-tracking datasets. Each frame of the fringe data, corresponding to one individual OPD setting inside a scan, is reduced to a one-dimensional spectrum by multiplying it with the mask and performing the weighted integral over the direction perpendicular to the spectral dispersion. Then the two – oppositely phased – interferometric output channels of the beam combiner are subtracted from each other. This combines the interferometric modulation of both channels into one and, at the same time, helps in subtracting out the background. The few dozen spectra from each scan with the piezo-mounted

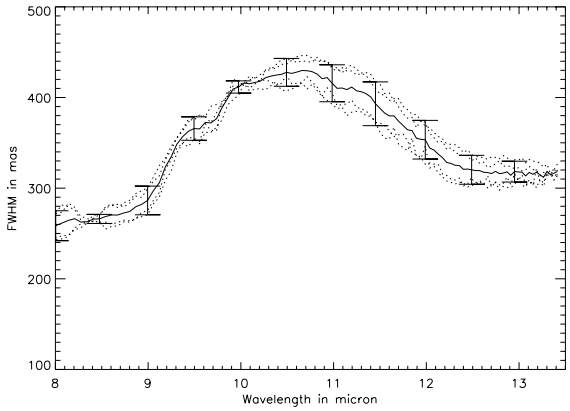

Fig. 5. Mean of *FWHM* curves of the star deconvolved spectra from UT3 (solid lines) and the individual deconvolution using different calibrators (dotted lines). The errors bars of the figure (spaced by 0.5 μm intervals) represent only the scatter of the measurements.

mirrors are collected into a two-dimensional array with optical wavelength and OPD as axes. The contents of this array are column-wise fourier-transformed from OPD to fringe frequency space. As a rule, four of the ≈0.05 μm wide wavelength (pixel) channels are added to improve the signal-to-noise (*S/N*) ratio. The fringe amplitude for each optical wavelength is then obtained from the power spectrum at the corresponding fringe frequency.

No correlated flux was detected with the UT1−UT3 projected baseline of 102.4 m at a PA angle of 39.6°. The atmospheric conditions and the data recorded during the fringe search were carefully checked. The seeing degraded slowly between 6 h and 8 h UT from 0.″4 to 0.″6 and standard deviation of the flux from the target pointed by the (visible) seeing monitor[2] increased also, which affected the observations of the bright calibrator HD 177716, though well below the cloud alert threshold. During the whole night, the atmospheric turbulence was quite rapid with a mean τ_0 = 3 ms. These atmospheric conditions, while not excellent, can still be considered as normal conditions at Paranal Observatory. Therefore the fringe detection threshold for MIDI during the observations OH 26.5+06 was nominal.

Based on the first few months of routine observations with MIDI, we can set limits on the amount of correlated flux the instrument is capable of detecting under average weather conditions. For instance, careful data reduction of the data from NGC 1068 shows that a correlated flux can be confidently detected down to 0.5 Jy for faint objects (Jaffe et al. 2004). For bright objects, visibilities of about 1% have been detected from the heavily resolved Herbig star HD 100546 (Leinert et al. 2004) or from the clumpy environment of the supergiant η Car (Chesneau et al. 2004). It is difficult to reach sensitivity less than 1% for bright objects because the beam combination is not perfect; a part of the noise residuals depends on the photometric noise from the bright source. This number has to be compared to photometric flux integrated over OH 26.5+0.6 of about 600−800 Jy. With the 100 m baseline, MIDI is sensitive to emission from any structure smaller than 10 mas exhibiting an integrated flux larger than 6−8 Jy in this case.

[2] This information was extracted from the ESO Ambient conditions database of Paranal observatory: `http://archive.eso.org/`

3. Modelling the circumstellar environment

3.1. The approach to modeling the object

Most of the studies on OH/IR stars and OH 26.5+0.6 in particular rely on interpretation of the observed variable Spectral Energy Distribution (SED) by comparing it to a synthetic SED, computed using a radiative transfer code. In this way, one tries to separate the effects of opacity and radial structure of the wind. Unfortunately, fits to the SED are often not unique, especially when deviations from spherical symmetry are taken into account. MIDI, however, provides a unique spectrally and spatially resolved data set that puts strong new constraints on any model for the envelope of OH 26.5+0.6. Below, we briefly outline the strategy used to fit the MIDI observations.

Despite convincing evidence that the envelope of OH 26.5+0.6 is not spherical, we begin our analysis assuming spherical symmetry. We use the SED observed by ISO to determine global envelope parameters. The ISO spectrum (and unfortunately also the IRAS data) was taken close to the star's minimum luminosity (Suh & Kim 2002); therefore the model fit provides some constraints on the physical parameters of the dust shell close to the minimum luminosity. The model fit parameters are compared to the parameters published by Justtanont et al. (1996), who also mainly scaled their spectrophotometric data to the minimum phase.

As a second step, we tried to find a good fit to the MIDI data alone (taken at maximum luminosity), i.e. without the help of any external spectrophotometric information as performed by Suh & Kim (2002). As a consequence, we tried to fit the MIDI spectrum by performing slight modifications to the minimum light model. Our goal was to check whether the MIDI spectrum can be fitted based on the previous model. As soon as a satisfactory fit was reached for the MIDI spectrum, we evaluate the spatial distribution of the flux predicted by the model and compare it with the extension at each wavelength measured by MIDI.

Finding the best model for a dust shell at maximum luminosity is such a complex study outside the scope of this paper that it is best left to a later paper dedicated to that purpose. Our goal was instead to pinpoint the kind of constraints provided by inclusion of the spectrum and spatial extension of the object in the process of model fitting and to demonstrate how new information can emerge about the dust content close to the star.

We use the radiative transfer code MODUST, commonly used for the SED fitting of this kind of star. The radiative transfer technique implemented in this code has been outlined by Bouwman (2001) and the specification of grain properties, such as size and shape distribution, is discussed in Bouwman et al. (2000).

Throughout this analysis, we adopt a distance of 1.37 kpc for OH 26.5+0.6. We note that distances to AGB stars are notoriously uncertain, and OH 26.5+0.6 is no exception.

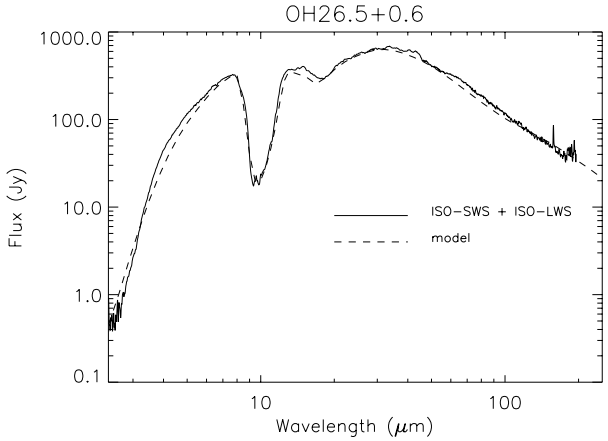

Fig. 6. Comparison between the ISO spectra (SWS + LWS) and a MODUST model using the JU96 parameters but with slightly reduced luminosity of the central star. Other differences are the use of CDE theory and inclusion of metallic iron. The crystalline features present in the ISO-SWS observations are not included in the model since they have little effect on the model structure (Kemper et al. 2002).

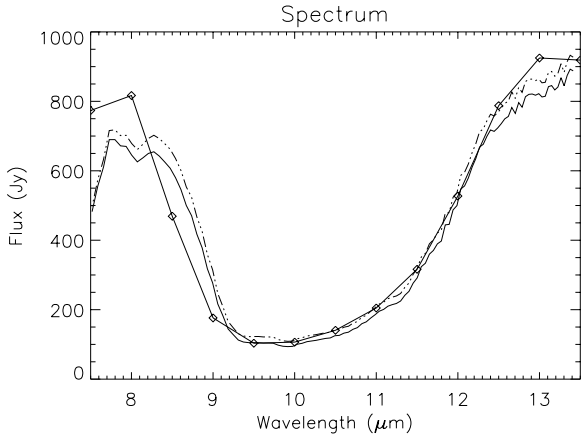

Fig. 7. Comparison between the MIDI spectrum (original: solid line, dereddened for IS extinction: dashed line) and the spectrum resulting from our ISO-tuned model but with increased central star luminosity (diamonds).

3.2. SED fit of OH 26.5+0.6 at minimum luminosity

JU96 constructed a model for OH 26.5+0.6 based on a large collection of photometry, spectroscopy, and CO-line measurements. Their 2-component model (a very thick inner shell, due to a recent superwind, surrounded by a tenuous AGB wind) shows that the near-mid IR is dominated by the superwind region. Most of their study is based on fluxes measured at minimum light, thus applicable to the ISO-SWS spectrum also obtained around minimum light (JD = 2 450 368, phase 0.47)

The superwind hypothesis is confirmed by the ISO-SWS spectrum, which shows very little far IR flux w.r.t. the depth of the 10 μm feature. Assuming a density distribution going as r^{-2}, this can be modelled only by cutting the shell fairly close to the star at a few hundred stellar radii instead of a few thousand.

Looking at the shape of the 9.7 μm feature, we can already improve on the composition of the dust. From its width and the location of the minimum, we conclude that CDE theory (CDE, Continuous Distribution of Ellipsoids) is to be preferred over spherical dust particles. Furthermore, there is strong evidence for the presence of metallic iron, as is the case for OH127.8+0.0 (Kemper et al. 2002); the slope in the (near-)IR (4−8 μm) cannot be explained without it. The flux blocked by the metallic iron in the near-IR emerges again in the Mid to Far-IR. Hence, the amount of Fe will significantly influence the optimum value of the other shell parameters.

The luminosity used by JU96 is by far too high for the epoch of these ISO-SWS observations. However, we do obtain a satisfying fit by reducing the stellar radius to 650 $R_\odot$ and keeping the outer radius at 8×10^{15} cm. The comparison model vs. ISO-SWS spectrum is shown in Fig. 6, where the general shape is approximately good. Most of the discrepancies can be attributed to the lack of crystalline dust in our model. The crystalline features present in the ISO-SWS observation are probably due to a few percent of enstatite and forsterite, but since these do not significantly influence the model structure[3], we do no detailed fitting of their spectral features.

Table 5. Model parameters from Justtanont et al. (1996) (JU96), and the same model adapted to minimum light (the ISO data, JD = 2 450 368, phase 0.47) and maximum light (the MIDI data, JD = 2 452 804, phase 0.06), dust evaporation scenario).

Param.	JU96	Minimum	Maximum
$T_{\rm eff}$ (K)	2200	2200	2100
$R_\star$ ($R_\odot$)	862	650	1100
Dist. (kpc)	1.37	1.37	1.37
Superwind			
$R_{\rm in}$ ($R_\star$)	7.5	7.5	20
$R_{\rm out}$ (cm)	8×10^{15}	8×10^{15}	8×10^{15}
$\dot{M}$ ($M_\odot$/yr)	5.5×10^{-4}	5.5×10^{-4}	8.5×10^{-4}
AGB wind			
$R_{\rm in}$ (cm)	8×10^{15}	8×10^{15}	8×10^{15}
$R_{\rm out}$ (cm)	5×10^{18}	5×10^{18}	5×10^{18}
$\dot{M}$ ($M_\odot$/yr)	$1. \times 10^{-6}$	1.4×10^{-5}	1.4×10^{-5}

3.3. Attempts to account for the MIDI data

Our model will have to explain the following new MIDI observations:

1. The MIDI N band spectrum taken close to the maximum light of OH 26.5+0.6 with the $0\farcs6 \times 2''$ slit.
2. The spatial extent of the spectrum. We limit ourselves to the comparison of the *FWHM* provided by a fit of the PSF-deconvolved MIDI spectrum by a 1D Gaussian compared with a similar fit of the model intensity profiles. The intensity distribution of OH 26.5+0.6 on the sky is very likely to be more complex than a simple Gaussian. However, it turned out to be difficult to disentangle imperfections in the imaging quality that resulted from the many reflections

[3] Their opacities are very similar to those of the amorphous material, Kemper et al. (2002).

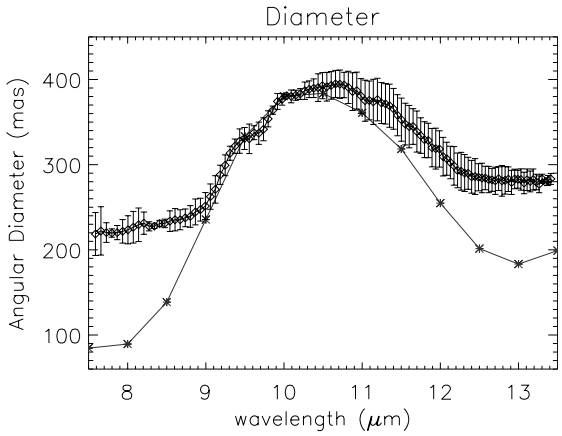

Fig. 8. A comparison between the *FWHM*s of the intensity profiles coming from the ISO-tuned model with a more luminous central star and the MIDI *FWHM*s. The predicted variation of diameter with wavelength is much larger than the one observed. Mainly the size at minimum optical thickness of the shell (at 8.5 and 13.5 μm) does not agree.

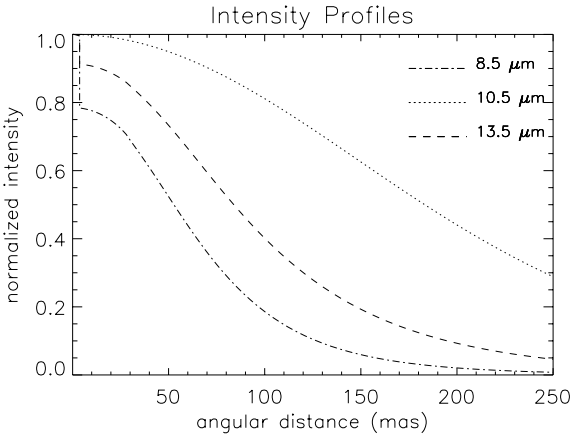

Fig. 9. Normalized intensity profiles for our model at maximum luminosity. In the wings of the 9.7 μm profile (at 8.5 and 13.5 μm), the shell optical thickness is only about 2 and thus the central star is visible. At 10.5 μm, the shell reaches an optical thickness of more than 10, resulting in the Gaussian intensity profile.

in the VLTI optical train to those intrinsic to the source, especially at lower intensity levels. The observed *FWHM* is attributed to a spherical object. The slit was oriented at PA = 72°, i.e. close to the maximum extension of the object.

3. Negative detection of fringes by MIDI. The constraints brought by this observational fact should not be underestimated. During maximum luminosity, the dust shell opacity is *at its minimum*. It is quite difficult for a model of the MIDI spectrum alone to disentangle models which are almost optically thin in the wings of the silicate features from the more optically thick ones. MIDI observations definitely discard any models of OH 26.5+0.6 for which the central star is visible with a (correlated) flux larger than 3−6 Jy through the shell at any wavelength located between 8 μm and 13.5 μm.

The MIDI observations were done very close to maximum light (JD = 2 452 804, phase 0.06), resulting in an observed flux that is more than twice as high compared to minimum light. In order to fit the model at minimum luminosity to the MIDI data at maximum luminosity, we must increase the total luminosity to $1.7 \times 10^4\ L_\odot$.

The increase in total luminosity is simulated by an increase of the central star diameter, still keeping the absolute value of the outer radius of the superwind fixed. Below we confront this model with the MIDI *FWHM* observations.

Figure 9 shows the spatial intensity profiles according to our ISO-tuned model adapted to the higher total luminosity at the time of the MIDI observations. The profiles at 8.5 and 13.5 μm correspond to a fairly low optical thickness of the shell, and thus the central star is not totally obscured. However, the amount of correlated flux by the central star is at most a few Jansky so close to the detection limit of MIDI (1% or 5−8 Jy). At 10.5 μm, the shell reaches an optical thickness of more than 10, resulting in the Gaussian intensity profile.

The *FWHM*s determined from these intensity profiles range from 100 mas to 370 mas (Fig. 8), clearly showing that if only the opacity by amorphous olivines were to determine the

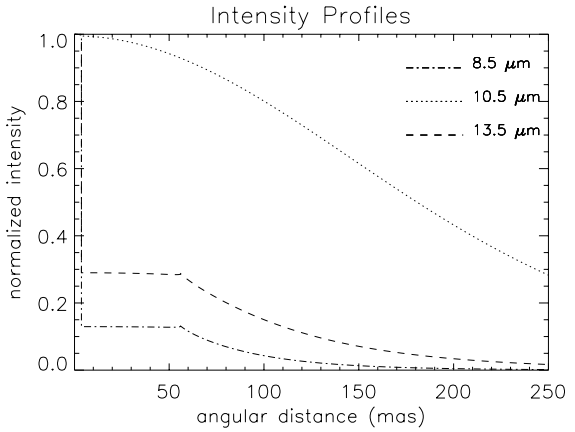

Fig. 10. Normalized intensity profiles for our model at maximum luminosity with an increased inner radius. For such intensity profiles, the inner radius determines the observed size of the object at wavelengths of low opacity.

diameter seen, the variations with wavelength would be much larger than what is observed. The maximum size appears to compare reasonably well with the model, though with a slightly different wavelength of maximum, and is compatible with the superwind size of JU96. More precisely, we can put a lower limit on the size of the superwind region of 400 mas, which corresponds to 4×10^{15} cm at 1.37 kpc.

The discrepancy between the spatial extent of the model and the observed size of the dust shell near 8 and 13 μm can be resolved if we move the inner radius of the dust shell farther from the star. The minimum size seen will be determined mainly by the inner radius of the dust shell; at the wavelengths of low optical depth, the intensity profile is not at all Gaussian (Fig. 10). In this way, the observed diameter in the wings of the 9.7 μm feature can be simulated by moving the inner radius out to about 20 $R_\odot$ (Fig. 11). For this model, a slightly higher mass loss ($8.5 \times 10^{-4}\ M_\odot$) is needed to keep the quality of the spectral fit.

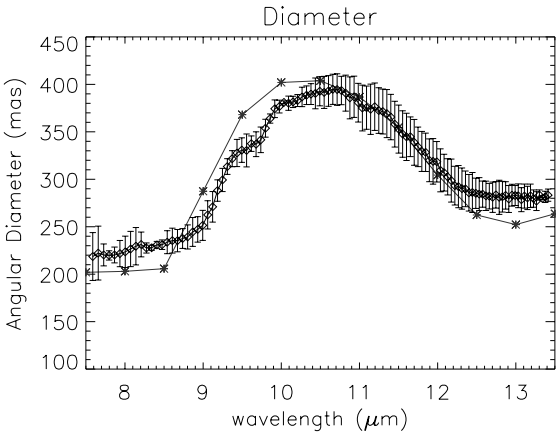

Fig. 11. Angular diameter fro our model compared to the MIDI data. The large observed radius at the red and blue sides of the profile can be simulated by moving the inner radius of the model far out, to about 20 $R_\star$.

At first sight, an alternative solution would be to introduce a source of opacity with only a modest wavelength dependence, which would dominate the silicate dust opacity near 8 and 13 μm. This could either be gas-phase molecular opacity or dust. However, by doing so the spectral fits become unacceptably poor, because the depth of the silicate feature can no longer be reproduced.

We conclude that the spectral and spatial data of OH 26.5+0.6 can be understood in the framework of a spherically symmetric shell with dust components that are also shown to be present in other OH/IR stars. The outer radius of the dust shell agrees well with the one estimated by Justtanont et al. (1996) as the radius of the onset of the superwind. The spatial data near 8 and 13 μm force us, in the context of spherical symmetry, to move the inner radius of the dust shell to a distance of about 20 stellar radii. However, this results in a predicted correlated flux using the 102 m UT1−UT3 baseline, which is 5 times the upper limit imposed by the non-detection of fringes in the interferometric signal (under the assumption that the central star has a typical AGB temperature of 3000−4000 K).

4. Discussion

4.1. Nature of the large inner dust radius

While a large inner radius of the dust shell seems a simple solution to our fitting problems, it is clearly not in agreement with the limits set by the interferometric measurement. In addition, such a large inner radius is not compatible with our current understanding of oxygen-rich AGB dust shells because the dust temperature at the inner edge of our dust envelope is only 500−600 K, well below what is believed to be the condensation temperature of olivines (1000 K). Furthermore, one can wonder whether the region between photosphere and olivine dust shell contains other material (refractory residuals of dust for instance, like corundum). Given the constraint that whatever fills this region must be quite transparent from 8 to 13 μm[4], several hypotheses can be formulated:

- a large cavity within this inner region could indicate that the mass loss has decreased strongly about 30 years ago. This is compatible with the timescales derived from the rings observed around several Post-AGB stars, hinting at episodic mass-loss with periods of a few hundred years (e.g. IRAS 17150-3224: Kwok 1998; IRC+10216: Mauron & Huggins 1999; Egg Nebula: Sahai 1998; Marengo 2001). However, stellar pulsations are quite regular and have been detected over the past 30 years (e.g. Suh & Kim 2002); so, if mass loss stopped, the pulsations apparently did not. Moreover, this model offers little opacity at 8 micron ($\tau_{8\ \mu\mathrm{m}}$ is of the order of 1) such that the amount of correlated flux from the central object would be about 5 times the detection limit of MIDI. This puts the relation between pulsations and mass loss for AGB stars in the superwind phase into question;
- the mass loss continues even today, and no condensation of the dust is possible inwards of 20 stellar radii when the star is at maximum luminosity. In fact, early dust condensation models by Sedlmayr (1989) have predicted that the dust condenses only when the gas is extremely super-saturated, which happens well below glass temperature, and would be around 800−600 K. Several other studies have previously hinted at the possibility that dust formation in AGBs does not happen close to the star. Danchi et al. (1994) also find some examples of stars with rather detached dust shells, corresponding to timescales of decades, so similar to what we find. However, other stars have inner dust radii much closer to the star;
- the dust gets periodically destroyed (dust evaporation), because the stellar luminosity changes during a pulsation cycle. Some calculations were done by Suh & Kim (2002), but do not predict the required amount of dust destruction to agree with our geometrical model. It is not certain that the net amount of dust created through an entire cycle is stable. This means that the episodical mass loss is a matter of balancing between destruction and formation. Of course, if the dust formation is not large enough to compensate for the evaporation, the inner gap would increase in size over multiple cycles.

It is by no means a straightforward choice between these possible explanations, and more importantly, not one of them explains the non-detection of fringes.

Although the SED is compatible with our spherically symmetric model, this assumption might be strongly violated, as suggested by the acquisition image. It is intuitively clear that a disk+bipolar outflow structure could account for the fitting problems we experienced. If the MIDI slit was oriented perpendicular to a nearly edge-on disk, the very high density (and thus opacity) would explain both the large size in the wings of

[4] This means optically thin from 7.5 to 9 micron and from 11.5 to 13.5 micron. An optically thick shell ($\tau \simeq 2-3$) would ruin the diameter profile since a smaller radius would be necessary to account for the SED.

the silicate feature and the non-detection of fringes. Because of the much larger complexity of 2D CSE modelling, we leave in-depth analysis of this hypothesis to a future paper dedicated to this question.

4.2. Star asymmetry

The drastic changes observed in the circumstellar structure of AGB and post-AGB stars are particularly puzzling. Information about the geometry of the AGB mass loss was first obtained from interferometry maps of OH 1612 Hz maser emission (Booth et al. 1981; Herman et al. 1985; Bowers & Johnston 1990). These, as well as CO radio line maps of a large number of AGB-stars (Neri et al. 1998; Olofsson et al. 1999, and references therein), were consistent with an over-all spherically symmetric mass loss. Evidence of deviation of the geometry of OH/IR stars can be found in the literature, but the results are usually somehow contradictory and perplexing due to the large range of masses and evolutionary stages encompassed by this term: from embedded AGBs to PPNs (van Winckel 2003). In particular, the sub-group of OH/IR star for which no pulsation can be detected is associated with PPNs (Zijlstra et al. 1991).

What makes the MIDI observations particularly interesting is that JU96 demonstrated that the star entered the superwind phase ∼200 yr ago. This provides an extremely short upper limit to the development of large scale asymmetry. For a large-mass star like OH 26.5+0.6, the duration of the OH/IR phase is expected to be on the order of 10^4 yr as compared to 10^3 yr for a low-mass star (JU96). Increasing evidence shows that AGB wind becomes axi-symmetric at the very last stages of the AGB evolution, and that the interaction with a fast wind by the post-AGB object further enhances the axi-symmetry. The MIDI observations suggest that, in the case of OH 26.5+0.6 the appearance of asymmetries can occur on a fairly short time scale (Sahai et al. 2003).

JU96 and Fong et al. (2002) reported CO observations that did not show any significant deviation from spherical symmetry for OH 26.5+0.6, but most of the emission is spatially unresolved (coming mostly from the superwind). In contrast, the OH 1612 Hz maser emission from Baud (1981) and Bowers & Johnston (1990) presents a clear picture of the clumpy and asymmetric environment OH 26.5+0.6. The radio shell of OH 26.5+0.6 is certainly one of the most extended and least symmetric known for OH/IR stars. The large scale environment of OH 26.5+0.6 is crowded, which does not ease the extraction of radio emission sensitive to any anisotropic UV radiation field, so that Bowers & Johnston (1990) proposed that it is a likely cause for the detected asymmetry.

The crucial point is that the axis of symmetry of the present Mid-IR objet is consistent with the large scale anisotropy detected in radio, which excludes a priori a strong external influence on the shaping of the OH maser. This correlation opens new possibilities for interpretation. In addition, Bowers & Johnston (1990) detected some hints of rotation at low projected velocity ($v_r < 3$ km s^{-1}) with a rotational axis aligned with the minor axis of the asymmetric shell.

What could be the origin of such asymmetry? This paper can hardly review all the mechanisms for explaining such a phenomenon so the reader is invited to consult the review of Balick & Frank (2002). We simply point out that OH 26.5+0.6 is not a known binary, but considering the difficulty of studying the central star of OH/IR star, this lack of detection is not significant. The discussion above lead us to think that the particular characteristics of OH 26.5+0.6 are perhaps better understood within the binarity hypothesis.

4.3. Improving the model

By using an up-to-date spherical model of a dust shell, we have been able to satisfactorily fit the SED of the star, but this model failed to provide a direct explanation of the non-detection of any fringes within the *N* band.

These difficulties point to a problem of opacities located in regions fairly close to the star though sufficiently extended to prevent detection of correlated flux by MIDI. One remedy is to make the radius of the central source larger so that almost no correlated fluxes can be detected by MIDI with a baseline as large as 100 m.

An attractive solution to this problem would to include molecular opacities. Growing evidence of their deep effects on interferometric measurements in the near and mid-infrared are reported (Matsuura et al. 2002; Mennesson et al. 2002; Perrin et al. 2004a,b; Schuller et al. 2004; Cotton et al. 2004; Ohnaka et al. 2004). The first effect is to increase the diameter of the central star and thus, to decrease the correlated flux. At maximum luminosity, the expected angular diameter OH 26.5+0.6 is about 8 mas (for $R_* = 1100\,R_\odot$) and the correlated flux from the central object should represent about 80% of the stellar flux if the star is a uniform disk. The inclusion of an optically thick molecular envelope of H_2O and SiO of about 2.5 R_* divides this correlated flux by 10, probably preventing its detection by MIDI. Moreover, the star can probably no longer be modelled by a uniform disk but by a spatially smoother flux distribution which again decreases the correlated flux. The second effect is to redistribute the flux from the central star to other regions of the spectrum. Of course, if the warm molecular layers are optically thick, they will emit like a blackbody at a temperature slightly lower than the star. The effects of this envelope on the dust formation/destruction processes have to be carefully evaluated and need consistent radiative transfer calculations, which are not in the scope of this paper.

Dust shell opacity remains an issue which could be solved by changing the dust density without affecting its composition or by adding species particularly absorptive between 8 and 13.5 μm. This implies either a very large olivine dust column density, or other highly absorptive dust species like corundum. An inner shell rich in metallic iron and corundum (Al_2O_3) could help to fit the observed extensions, by preventing the flux from the star to be detected. The corundum is used, for instance, to model the opacities of the thin dust shell around some Miras, with mass ratio of corundum to silicate ranging from 0.6 to 0.9 and grain sizes of 0.1−0.2 μm (Martin-Lorenz & Pompeia 2000; Ohnaka et al. 2004). However, the amount

of material needed is limited by the natural abundance of Al in the photosphere. In our first tests, this needed amount is at the moment unrealistically high to prevent the correlated flux from the star to be detected, under the hypothesis that the star is a naked photosphere of about 1100 $R_{\odot}$ at 2100 K (i.e. a uniform disk).

Finally, for the sake of simplicity, we have put all the discussions in the frame of a spherical object. All the codes used to model the SED of OH 26.5+0.6 have been using spherical geometry to understand an object which is proven to be strongly flattened in this article.

For the sake of simplicity, we based our discussions on a spherical object. Previous work, based on radiative transfer code that tries to model the SED of OH 26.5+0.6 have also used spherical geometry to help understand this object. As seen above, however, it is much too flattened for this to be that simple.

A very promising hypothesis is that we are indeed observing a high olivine column density in direction perpendicular to the slit, i.e. that we are looking at equatorial overdensity (or even a disk) close to an edge-on configuration, which explains the large aspect ratio of the 8.7 μm MIDI image.

4.4. Envelope clumping

The fact that no fringes have been detected from OH 26.5+0.6 implies also that the dusty environment of OH 26.5+0.6 is relatively homogeneous and smooth. Most of the flux originates in the dust shell and the absence of fringes contrasts strongly with the almost ubiquitous fringes found around the massive star Eta Car in an area as large as $0\farcs6 \times 0\farcs6$ with photometric fluxes comparable to the ones reported here (Chesneau et al. 2005). Using continuous dust distribution for modelling this kind of environment is thus fully justified.

Pulsations are supposed to generate a strongly clumped medium due to the shocks, but Suh et al. (1990) have shown that this region is limited to the 3 R_*. The rapid outward acceleration extending to 10−20 R_* should considerably smooth out the dusty wind. In the Suh et al. model, the dust condensation radius is about 6 R_* depending on the pulsation phase. Even considering the pulsation, their model of the dusty envelope is very close to a smooth r^{-2} density law. The clumpy regions embedded in the optically thick part of the shell at 10 μm should not be visible, but some signal could be expected at 8 or 12 μm at maximum luminosity if the dust shell is sufficiently optically thin. The clumps are probably embedded in the putative optically thick molecular layer so that their correlated emission would be largely hidden and therefore undetectable by MIDI.

5. Conclusion

The dust model used to interpret the SED from OH 26.5+0.5 in this article has been shown unable to predict the large extension of the dust shell outside the silicate absorption region, while also maintaining a sufficient level of opacity to render the flux from the central object undetectable by MIDI. That these two complementary constraints occur in conjunction means we must make a more concerted effort to understand the physical processes operating at the inner regions of the dust shell. OH 26.5+0.6 is indeed a very complex object that exhibits a wide range of physical phenomena:

- A asymmetric appearance, whose axis of symmetry is probably coincident with the axis of rotation of the star.
- A thick dust envelope whose characteristics are modulated by the pulsation cycle.
- A complex inner shell where dust forms and is destroyed throughout the cycle. The contribution of corundum and metallic iron opacities in this region are probably important.
- A putative thick molecular envelope as encountered in many, if not all, Mira stars which increases the angular diameter of the central star and decreases the apparent temperature.

The results presented in this paper are very constraining and have to be confronted with a model able to consistently handle the complex interplay between the pulsating central star, its molecular atmosphere and the mechanisms of dust formation/destruction and transport. However, such a theoretical approach is, at the moment, inefficient until confirmation of the presence of a disk around this object allows a restricted range of geometrical parameters.

In the course of the ∼1560 days of its cycle, MIDI/VLTI interferometer allows continuing monitoring of OH 26.5+0.6. The observations will provide a unique view of the evolution of the size and shape of the dusty envelope throughout the entire cycle. However the phase of maximum luminosity remains the only opportunity to reach the internal regions closest to the star.

High resolution observations in optical and near-infrared by means of Adaptive Optics should also help to estimate the amount of scattered light close to the object in order to efficiently test the disk hypothesis.

Acknowledgements. We acknowledge fruitful discussion with Carsten Dominik and Ciska Kemper. O.C. acknowledges the Max-Planck Institut für Astronomie in Heidelberg, Germany and in particular Christoph Leinert and Uwe Graser for having given him the opportunity to work at a motivating project within a rich scientific environment.

References

Arenou, F., Grenon, M., & Gomez, A. 1992, A&A, 258, 104
Balick, B., & Frank, A. 2002, ARA&A, 40, 439
Baud, B. 1981, ApJ, 250, L79
Bouwman, J. 2001, Ph.D. Thesis, University of Amsterdam
Bouwman, J., de Koter, A., van den Ancker, M. E., & Waters, L. B. F. M. 2000, A&A, 360, 213
Bowers, P. F., & Johnston, K. J. 1990, ApJ, 354, 676
Bujarrabal, V., García-Segura, G., Morris, M., et al. 2000, ASP Conf. Ser., 199, 201
Chesneau, O., Min, M., Herbst, T., et al. 2005, A&A, accepted
Chevalier, R. A., & Luo, D. 1994, ApJ, 421, 225
Cobb, M. L., & Fix, J. D. 1987, ApJ, 315 325
Cohen, M., Walker, R. G., Carter, B., et al. 1999, AJ, 117, 1864
Corradi, R. L. M., & Schwarz, H. E. 1995, A&A, 293, 871

Cotton, W. D., Mennesson, B., Diamond, P. J., et al. 2004, A&A, 414, 275
Dick, H. M., Zuckerman, B., Leinert, Ch., & Beckwith, S. 1984, ApJ, 287, 801
Fix, J. D., & Cobb, M. L. 1988, ApJ, 329, 290
Fong, D., Justtanont, K., Meixner, M., & Campbell, M. T. 2002, A&A, 396, 581
Habing, H. J. 1996, A&ARv, 7, 9
Heske, A., Forveille, T., Omont, A., et al. 1990, A&A, 239, 173
Herman, J., Baud, B., Habing, H. J., & Winnberg, A. 1985, A&A, 143, 122
Iben, I., & Renzini, A. 1983, ARA&A, 21, 271
Icke, V., Preston, H. L., & Balick, B. 1989, AJ, 97, 462
Jaffe, W., Meisenheimer, K., & Röttgering, H. J. A. 2004, Nature, accepted
Jones, T. J., & Gehrz, D. 1990, AJ, 100, 274
Johnson, J., & Jones, T. J. 1991, AJ, 101, 1735
Justtanont, K., Skinner, C. J., & Tielens, A. G. G. M. 1994, ApJ, 435, 852
Justtanont, K., Skinner, C. J., Tielens, A. G. G. M., Meixner, M., & Baas, F. 1996, ApJ, 456, 337
Kemper, F., Waters, L. B. F. M., de Koter, A., & Tielens, A. G. G. M. 2001, A&A, 369, 132
Kemper, F., De Koter A., Waters, L. B. F. M., et al. 2002, A&A, 384, 585
Kwok, S., Su, K. Y. L., & Hrivnak, B. J. 1998, ApJ, 501, L117
Leinert, Ch., Graser, U., Waters, L. B. F. M., et al. 2003a, SPIE, 4838, 893
Leinert, Ch., Graser, U., & Przygodda, F. 2003b, Ap&SS, 286, 73
Leinert, Ch., van Boekel, R., Waters, L. B. F. M., et al. 2004, A&A, accepted
Martin-Lorenz, S., & Pompeia, L. 2000, MNRAS, 315, 856
Marengo, M., Ivezic, Z., & Knapp, G. R. 2001, MNRAS, 324, 1117
Mariotti, J.-M., Chelli, A., Foy., R., et al. 1983, A&A, 120, 237
Matsuura, M., Yamamura, I., Cami, J., et al. 2002, A&A, 383, 972
Mauron, N., & Huggins, P. J. 1999, A&A, 349, 203
Mennesson, B., Perrin, G., Chagnon, G., et al. 2002, APJ, 579, 446
Molster, F. J., Waters, L. B. F. M., Tielens, A. G. G. M., & Barlow, M. J. 2002, A&A, 382, 184
Monnier, J. D., Millan-Gabet, R., Tuthill, P. G., et al. 2004, ApJ, 605, 436
Ohnaka, K., Bergeat, J., Driebe, T., et al. 2004, A&A, submitted
Perrin, G., Ridgway, S. T., Coudé du Foresto, V., et al. 2004, A&A, 418, 675
Perrin, G., Ridgway, S. T., & Mennesson, B. 2004, A&A, submitted
Przygodda, F., Chesneau, O., Graser, U., et al. 2003, Ap&SS, 286, 85
Sahai, R., Trauger, J. T., & Watson, A. M. 1998, ApJ, 493, 301
Sahai, R. 2000, ASP Conf. Ser., 199, 209
Sahai, R., Morris, M., Sanchez Contreras, C., & Claussen, M. 2003, A&AS, 203, 1104
Savage, B. D., & Mathis, J. S. 1979, ARA&A, 17, 73
Schuller, P., Salomé, P., Perrin, G., et al. 2004, A&A, 418, 151
Suh, K.-W., Jones, T. J., & Bowen, G. H., ApJ, 358, 588
Suh, K.-W., & Kim, H.-Y. 2002, A&A, 391, 665
Starck, J.-L., Bijaoui, A., Lopez, B., & Perrier, C. 1994, A&A, 283, 349
Sylvester, R. J., Kemper, F., Barlow, M. J., et al. 1999, A&A, 352, 587
te Lintel Hekkert, P., Versteege-Hensel, H. A., Habing, H. J., et al. 1989, A&AS, 78, 399
van Winckel, H. 2003, ARA&A, 41, 391
Wilson, W. J., & Barrett, A. H. 1972, A&A, 17, 385
Zijlstra, A. A., Chapman, J. M., te Lintel Hekkert, P., et al. 1991, A&A, 243, L9
Zijlstra, A. A., Chapman, J. M., te Lintel Hekkert, P., et al. 2001, MNRAS, 322, 280